

This work was written as part of one of the author's official duties as an Employee of the United States Government and is therefore a work of the United States Government. In accordance with 17 U.S.C. 105, no copyright protection is available for such works under U.S. Law.

Public Domain Mark 1.0

<https://creativecommons.org/publicdomain/mark/1.0/>

Access to this work was provided by the University of Maryland, Baltimore County (UMBC) ScholarWorks@UMBC digital repository on the Maryland Shared Open Access (MD-SOAR) platform.

Please provide feedback

Please support the ScholarWorks@UMBC repository by emailing scholarworks-group@umbc.edu and telling us what having access to this work means to you and why it's important to you. Thank you.

Iron and Nickel fluxes measured by CALET on the International Space Station

Francesco Stolzi,^{a,b,*} Caterina Checchia,^{a,b} Gabriele Bigongiari,^{a,b} Yosui Akaike^{c,d}
for the CALET collaboration

^a*Department of Physical Sciences, Earth and Environment,
University of Siena, via Roma 56, 53100 Siena, Italy*

^b*INFN Sezione di Pisa,
Polo Fibonacci, Largo B. Pontecorvo, 3, 56127 Pisa, Italy*

^c*Waseda Research Institute for Science and Engineering,
Waseda University, 17 Kikucho, Shinjuku, Tokyo 162-0044, Japan*

^d*JEM Utilization Center, Human Spaceflight Technology Directorat, Japan Aerospace Exploration Agency,
2-1-1 Sengen, Tsukuba, Ibaraki 305-8505, Japan*

*E-mail: francesco.stolzi@unisi.it, caterina.checchia2@unisi.it,
yakaika@aoni.waseda.jp, gabriele.bigongiari@unisi.it*

The study of the spectral behavior of heavy cosmic-ray elements may shed light on the details of propagation and acceleration phenomena in our Galaxy. The CALorimetric Electron Telescope (CALET) is measuring the spectra of heavy nuclei up to the highest directly observed energies on the International Space Station. In this contribution, based on the data collected during 7 years of operation, the measurement of the energy dependence of iron and nickel fluxes is presented. With respect to our previous published measurements, the analysis has been extended to a data sample enriched with more than 2.5 (1.5) extra years for iron (nickel). The results of the new analysis are reported together with a detailed assessment of systematic uncertainties. In the energy range explored so far, both spectra show a similar shape and energy dependence, suggesting that iron and nickel may follow almost identical acceleration and propagation mechanisms.

38th International Cosmic Ray Conference (ICRC2023)
26 July - 3 August, 2023
Nagoya, Japan



*Speaker

1. Introduction

Direct measurements of charged CR have revealed important spectral features such as a hardening in the heavy and light nuclei spectra around a few hundred GeV/n [1–13], but also a softening in the proton and helium spectra above the TeV region [14–16]. Iron and nickel nuclei provides favorable conditions for observations thanks to largest relative abundance (among the heavy elements) and negligible contamination from spallation of higher mass elements. The CALorimetric Electron Telescope (CALET) [17–20], a space-based instrument optimized for the measurement of the all-electron spectrum, reported results of the electron spectrum [21, 22] and of the light and heavy nuclei spectra [5, 6, 14, 15, 23, 24] including the iron and nickel spectra. It is equipped with a thick homogeneous calorimeter with excellent capabilities to measure the hadronic component of cosmic rays including proton, light, and heavy nuclei (up to nickel and above) in the energy range up to 1 PeV. In this paper we present the updated analysis of iron and nickel flux measurements based on the data collected by CALET from November 1, 2015 to December 31, 2022 aboard the International Space Station (ISS).

2. CALET instrument

CALET is an all-calorimetric instrument, consisting of three main subdetectors: on the top a pair of plastic scintillator hodoscopes acting as CHarge Detector (CHD), in the middle a finely segmented pre-shower IMaging Calorimeter (IMC) and at the end 27 X_0 thick Total AbSorption Calorimeter (TASC). The CHD identifies the charge from $Z = 1$ to $Z = 40$ with excellent resolution. An independent charge measurement, via multiple samples of specific energy loss (dE/dx) in each fiber is also provided by IMC up to the onset of saturation which occurs for ions more highly charged than silicon. The CR particle direction is reconstructed by IMC, made of 16 layers of thin scintillating fibers read out individually. The particle's energy is measured with the TASC, a lead-tungstate homogeneous calorimeter of 27 radiation lengths and 1.2 proton interaction lengths. The instrument was launched on August 19, 2015, and placed on the JEM EF (Japanese Experiment Module Exposed Facility) on the ISS. Scientific observations [25] started on October 13, 2015, and smooth and continuous operations have taken place since then. Calibration and test of the instrument took place at the CERN-SPS during five campaigns between 2010 and 2015 with beams of electrons, protons, and relativistic ions. The TASC response was studied at CERN SPS in 2015 using a beam of accelerated ion fragments with $A/Z = 2$, obtained with a primary beam of ^{40}Ar nuclei, and kinetic energy of 13, 19 and 150 GeV/c/n [26]. The energy response was found to be linear up to the maximum particle energy of 6 TeV. Furthermore, it was found that the mean energy released in the TASC is $\sim 20\%$ of the particle energy and the resolution is $\sim 30\%$. Monte Carlo (MC) simulations, based on the EPICS simulation package [27], were used to reproduce the detailed detector configuration, physical processes, as well as detector signals and to evaluate event reconstruction efficiencies, background contaminations and the energy response matrix. On the other hand, simulations based on GEANT4 [28] are used for an independent iron analysis and to evaluate the systematic uncertainties for nickel analysis.

3. Data Analysis

We analyzed a period of 2618 days of flight data (FD) for the present analysis. The total observation live time for the high-energy (HE) shower trigger is $T \sim 5.3 \times 10^4$ h, corresponding to $\sim 86\%$ of total observation time. As mentioned above, the nickel analysis is based on EPICS MC simulations, while for the iron we report two different analysis based both on EPICS and GEANT4 up to 1000 GeV/n. Nickel analysis is the same as reported in ref [23], but with a statistics increased by 1.3 times. For iron, on the other hand, the analysis has also been updated from that in [24] by expanding the acceptance to that of nickel and expanding the charge selection.

Raw signals are corrected for gain differences among the channels, position and temperature dependence, temporal gain variations as well as non-uniformity in light output. The HE trigger, based on the coincidence of the summed signals of the last four IMC layers and the top TASC layer, is fully efficient (close to 100%) for elements heavier than oxygen. Thus, in order to select interacting Ni and Fe candidates, a deposit larger (2 sigmas) than the minimum ionization particle (MIP) peak is required in at least one of the first four layers of the TASC (*shower event cut*). Events with a well-fitted primary track crossing the detector from CHD top to TASC bottom and clear from the edges of TASCX1 by at least 2 cm are used for this analysis. The fiducial geometrical factor results $S\Omega \sim 510 \text{ cm}^2 \text{ sr}$. The resolution of the impact point on CHD is $\sim 180 \mu\text{m}$, whereas angular resolution is $\sim 0.08^\circ$ both for Fe and Ni nuclei.

The signals of the CHD paddles traversed by the incident particle and corrected for its path length are used to reconstruct the particle's charge Z : two charge values (Z_{CHDX} , Z_{CHDY}) are reconstructed. In fact either CHD layer provides an independent dE/dx measurement which is corrected for the quenching effect in the scintillator's light yield. Both CHD signals are affected by additional energy deposit due to backscattered shower particles from the TASC at higher energy. This results in a systematic displacement of the CHDX and CHDY charge peaks to higher values with respect to the nominal charge position. Therefore it is necessary to restore the peak position to its nominal value by an energy dependent charge correction applied separately to the FD and the MC data. The increase in statistics allowed greater precision in correcting for this effect. Residual background due to charge-changing nuclear interactions occurring in the upper part of the instrument is removed by requiring that the difference between the charges from either layer of the CHD is less than 1.5 charge units. A charge distribution obtained by averaging Z_{CHDX} and Z_{CHDY} is shown in Fig.1. The CHD charge resolutions σ_Z of the combined CHD layers are $0.35e$ and $0.39e$ (in charge units) for iron and nickel, respectively. Iron (nickel) candidates are identified by an ellipse centered at $Z = 26$ (28), with $2(1.4)\sigma_x$ and $2(1.4)\sigma_y$ wide semiaxes for Z_{CHDX} and Z_{CHDY} , respectively, and rotated clockwise by 45° as shown in the cross plot of the CHDY vs CHDX charge in Fig. 2. After the cuts mentioned above, 6.4×10^3 Ni and 1.2×10^5 Fe candidate events are identified.

The shower energy E_{TASC} of each event is calculated as the sum of the energy deposits of all TASC logs after merging the gain ranges of each channel [29]. The 2015 beam test results [26] were used to tune the energy response derived from MC simulations [5]. The TASC crystals are subject to a phenomenon of light quenching for nuclei with a $Z > 10$, that is not reproduced by the MC simulations. This requires an *a posteriori* correction, obtained from the flight data, to the MC energy deposits generated in the TASC logs by noninteracting primary particles [24].

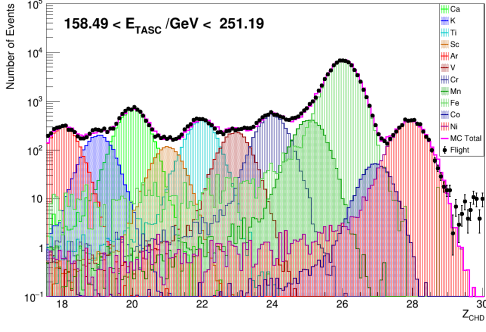


Figure 1: Charge distributions from the combined charge measurement of the two CHD layers. Flight data, represented by black dots, are compared with Monte Carlo samples including argon, potassium, calcium, scandium, titanium, vanadium, chromium, manganese, iron, cobalt and nickel.

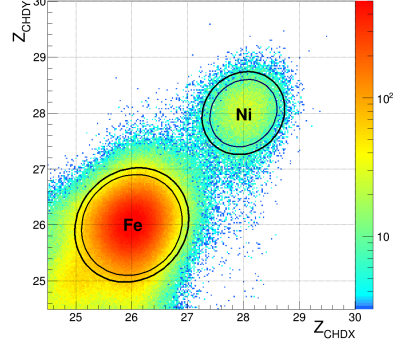


Figure 2: Crossplot of Z_{CHDY} vs. Z_{CHDX} reconstructed charges. The maximum and the minimum elliptical selection for the iron and nickel candidates are indicated by the ellipses in the figure.

In order to obtain the flux measurement, energy unfolding is applied to correct E_{TASC} distributions for bin-to-bin migration effects, due to the limited energy resolution, and infer the primary particle energy. The response matrix is derived using MC simulation after applying the same selection procedure as for flight data. In this analysis, the Bayesian approach [30] implemented within the RooUnfold package [31] was used. The energy spectrum is obtained from the unfolded energy distribution as follows:

$$\Phi(E) = \frac{N(E)}{\Delta(E)\epsilon(E)S\Omega T}; \quad N(E) = U[N_{obs}(E_{TASC}) - N_{bg}(E_{TASC})] \quad (1)$$

where $S\Omega$ denotes the geometrical factor, T is the live time, E is the geometric mean of the lower and upper bounds of the bin, $\Delta(E)$ is the energy bin width, $N(E)$ identifies the bin content in the unfolded distribution, $\epsilon(E)$ is the total selection efficiency [23, 24], $U()$ identifies the unfolding procedure operator, $N_{obs}(E_{TASC})$ denotes the bin content of observed energy distribution (including background), and $N_{bg}(E_{TASC})$ is the bin content of background events in the observed energy distribution. The contamination for Ni is mainly due to the iron background: it results $< 1\%$ in the energy range between 10^2 and 10^3 GeV and it increases up to 10% at $\sim 10^4$ GeV. The contamination for Fe, mainly due to the Mn background, is similar to that of Ni up to 10^3 GeV increasing up to $\sim 2\%$ at $E_{TASC} \sim 10^4$ GeV.

4. Systematics errors

The Fig. 3 (a) and (b) shows a breakdown of the energy-dependent systematic errors for nickel and iron when EPICS is used as MC. They come from several sources and include, MC GEANT4 model (only for nickel), charge identification, beam test configuration, energy scale correction, shower event shape and energy unfolding.

By varying the semi-minor and major axes of the elliptical selection up to 15% (50%) for Ni (Fe), the systematic error associated with charge identification was investigated. With the increase in statistics, this systematic has been reduced to a maximum of 5% for Ni and 6% for Fe.

When GEANT4 is used instead of the EPICS simulation, the resulting Ni flux show a maximum discrepancy of about 10% in the 100-200 GeV/n region. The uncertainties due to the unfolding procedure were calculated with different response matrices computed by varying the spectral index (between -2.9 and -2.2) of the MC generation spectrum. The uncertainty on the energy scale correction is $\pm 2\%$ and causes a rigid shift of the measured energies, affecting the absolute flux normalization by $^{+3.3\%}_{-3.2\%}$ ($\pm 4\%$) for Fe (Ni) but not the spectral shape. Also, the contributions due to the beam test model and the shower event cut are included in the systematic uncertainties. Systematic error related to isotopic composition was evaluated in the nickel analysis since only ^{58}Ni isotope was considered. This reduces the normalization by 2.2%. Systematic energy-independent uncertainties affecting flux normalization include lifetime (3.4%), long-term stability ($< 2\%$ for Fe, $< 3\%$ for Ni), and geometric factor ($\sim 1.6\%$). The total systematic error is computed as the quadrature sum of all the sources of systematics in each energy bin. A preliminary study of the energy-dependent systematic errors for iron when GEANT4 is used instead of EPICS is also computed: the total systematic error is found to be well within 10% in all the energy range.

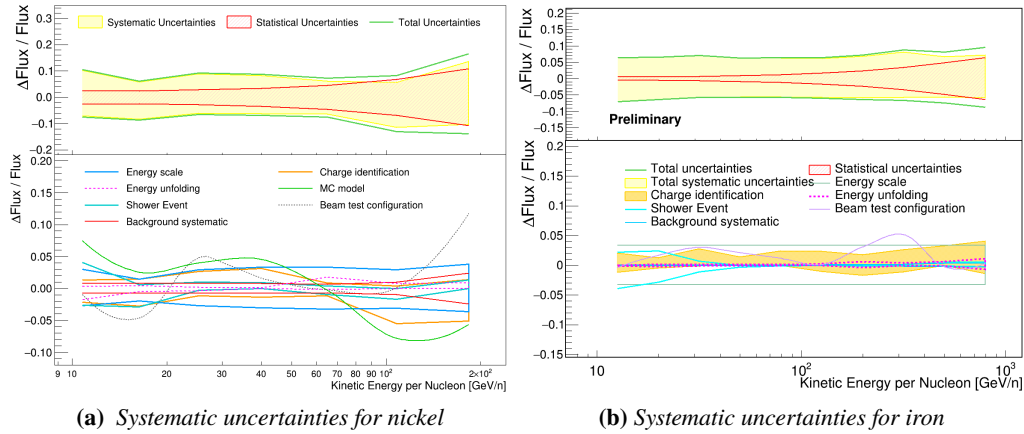


Figure 3: Energy dependence (in GeV/nucleon) of systematic uncertainties for nickel (a) and iron (EPICS) (b). On the top panel the band bounded by the red lines represents the statistical error. The shaded yellow band shows the sum in quadrature of all the sources of systematics including energy independent ones. The green lines represent the sum in quadrature of statistical and total systematic uncertainties. On the bottom panel the energy dependent sources of systematics errors are shown.

5. Results

Fig. 4 (a) shows the nickel spectrum in kinetic energy per nucleon measured by CALET in the energy range from 8.8 GeV/n to 240 GeV/n. Here, the statistics are increased by a factor of 1.3 compared to the previous publication [23]. Fig. 4 (b) shows the preliminary iron spectrum in kinetic energy per nucleon measured by CALET in the energy range from 10 GeV/n to 1000 GeV/n. In this case, the statistics are increased by a factor of 2 compared to the previous publication [24]. Fig. 4 (c) shows the iron GEANT spectrum obtained by the same procedure used for the one based on EPICS. The two iron spectra are consistent above 100 GeV/n, while differ in normalization in the low energy region about 10%. This difference can be attributed to the response matrices, which differ significantly in the low-energy region.

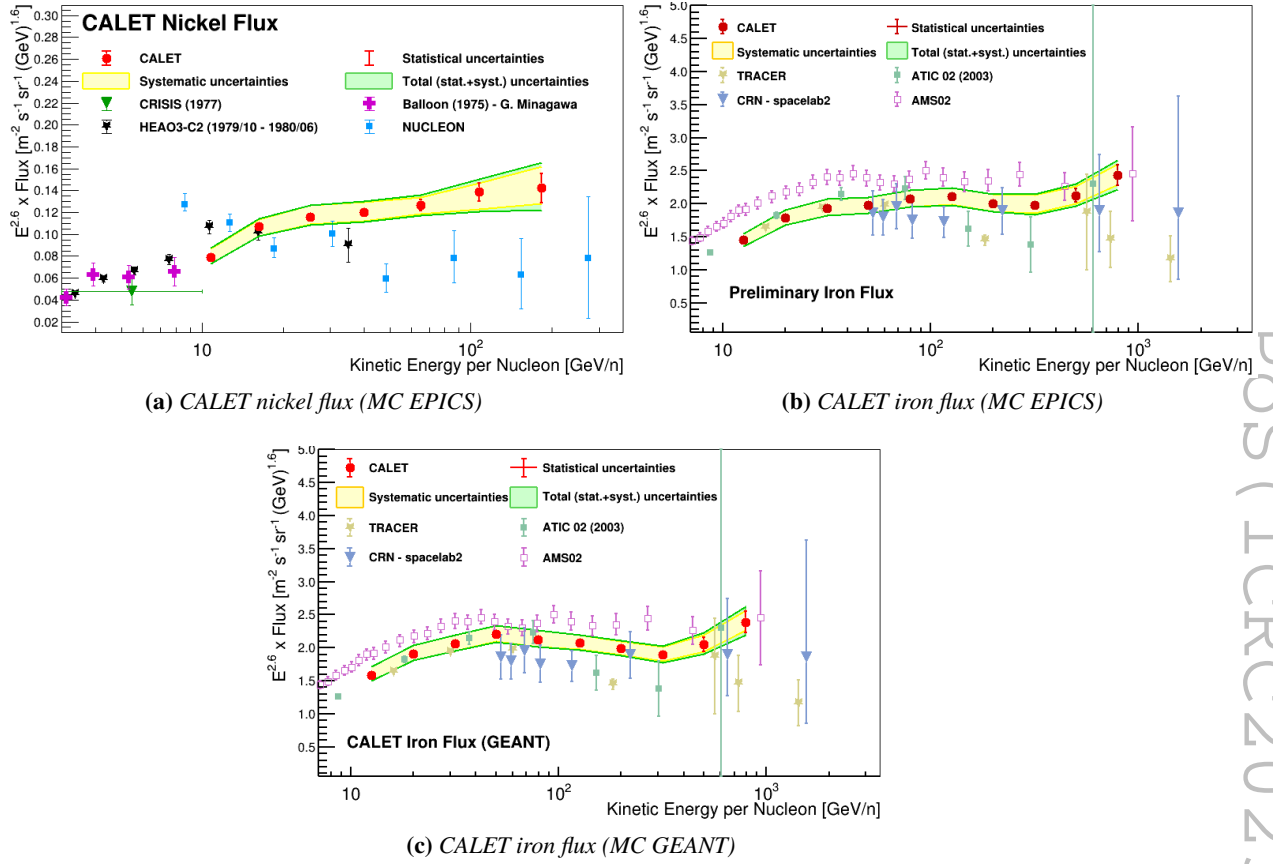


Figure 4: CALET nickel (a), iron EPICS (b) and iron GEANT4 (c) fluxes (multiplied by $E^{2.6}$) as a function of kinetic energy per nucleon. Error bars of the CALET data (red) represent the statistical uncertainty only, the yellow band indicates the quadrature sum of systematic errors, while the green band indicates the quadrature sum of statistical and systematic errors. Also plotted are other direct measurements [32–39].

Fig. 5 (a) shows the fit to the CALET Fe flux with a double power-law (DPL) function:

$$\begin{cases} \Phi(E) = C \left(\frac{E}{\text{GeV}} \right)^\gamma & E < E_0 \\ \Phi(E) = C \left(\frac{E}{\text{GeV}} \right)^\gamma \left(\frac{E}{\text{GeV}} \right)^{\Delta\gamma} & E > E_0 \end{cases} \quad (2)$$

where C is a normalization factor, γ the spectral index, and $\Delta\gamma$ the spectral index change above the transition energy E_0 . A single power-law function (SPL) $\Phi(E) = C \left(\frac{E}{\text{GeV}} \right)^\gamma$ is also shown for comparison. The DPL fit, performed from 50 GeV/ n to 1000 GeV/ n , gives a $\gamma = -2.60 \pm 0.01$ (stat) ± 0.08 (sys), $\Delta\gamma = 0.29 \pm 0.27$ and $E_0 = (428 \pm 314) \text{ GeV}/n$ with $\chi^2/d.o.f = 0.82/3$. The SPL fit in the same energy range gives $\gamma = -2.56 \pm 0.01$ (stat) ± 0.03 (sys) with $\chi^2/d.o.f = 2.7/5$. The significance of the fit with the DPL in the studied energy range is not sufficient to exclude the possibility of a single power law. Fig. 5 (b) shows the fit to the CALET Ni flux with a SPL function performed from 20 GeV/ n to 240 GeV/ n . The fit result gives $\gamma = -2.49 \pm 0.03$ (stat) ± 0.07 (sys) with $\chi^2/d.o.f = 0.1/3$. This result shows that the Ni flux, in the fit region, is compatible within the errors with a single power law.

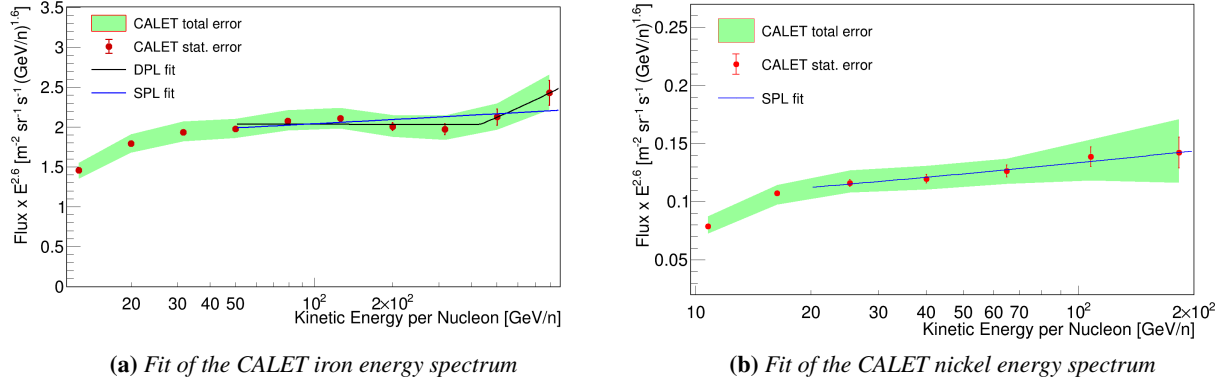


Figure 5: (a) Fit of the CALET iron energy spectrum to an SPL function (blue line) and to an DPL function (black line) in the energy range 50 GeV/n to 1000 GeV/n. (b) Fit of the CALET nickel energy spectrum to an SPL function (blue line). The fluxes are multiplied by $E^{2.6}$ where E is the kinetic energy per nucleon. The error bars are representative of purely statistical errors.

6. Conclusion

We report a measurement of the energy spectra of iron and nickel from 10 to 1000 GeV/n and from 8.8 to 240 GeV/n, respectively increasing the previous statistics by 1.3 times for Ni and 2 times for Fe. We also report a preliminary analysis of iron flux based on GEANT4 instead of EPICS. The nickel spectrum, as reported in our previous publication [23], is consistent with the hypothesis of an SPL with a spectral index of $\gamma = -2.49 \pm 0.08$. The iron flux based on GEANT4 is consistent with that based on EPICS above 100 GeV/n, while differ in normalization in the low energy region about 10%. The preliminary fit with a DPL performed on the iron spectrum up to 1000 GeV/n does not yet allow to draw a significant conclusion on a possible hardening. Extending the new iron analysis to an energy above some TeV/n may provide more precise information about a possible deviation from SPL.

Acknowledgements

We gratefully acknowledge JAXA's contributions to the development of CALET and to the operations onboard the International Space Station. The CALET effort in Italy is supported by ASI under Agreement No. 2013-018-R.0 and its amendments. The CALET effort in the United States is supported by NASA through Grants No. 80NSSC20K0397, No. 80NSSC20K0399, and No. NNH18ZDA001N-APRA18-0004. This work is supported in part by JSPS Grant-in-Aid for Scientific Research (S) Grant No.19H05608 in Japan.

References

- [1] M. Aguilar et al. *Phys. Rev. Lett.* **119** (2017) 251101.
- [2] M. Aguilar et al. *Phys. Rev. Lett.* **120** (2018) 021101.
- [3] M. Aguilar et al. *Phys. Rev. Lett.* **124** (2020) 211102.
- [4] H.S. Ahn et al. *Astrophys. J. Lett.* **714** (2010) L89.
- [5] O. Adriani et al. *Phys. Rev. Lett.* **125** (2020) 251102.

- [6] O. Adriani et al. *Phys. Rev. Lett.* **129** (2022) 251103.
- [7] M. Aguilar et al. *Phys. Rev. Lett.* **114** (2015) 171103.
- [8] M. Aguilar et al. *Phys. Rev. Lett.* **115** (2015) 211101.
- [9] O. Adriani et al. *Science* **332** (2011) 69.
- [10] Y.S. Yoon et al. *Astrophys. J.* **722** (2011) 122.
- [11] Y.S. Yoon et al. *Astrophys. J.* **839** (2017) 5.
- [12] Q. An et al. *Sci. Adv.* **5** (2019) eaax3793.
- [13] O. Adriani et al. *Phys. Rev. Lett.* **122** (2019) 181102.
- [14] O. Adriani et al. *Phys. Rev. Lett.* **129** (2022) 101102.
- [15] O. Adriani et al. *Phys. Rev. Lett.* **130** (2023) 171002.
- [16] F. Alemanno et al. *Phys. Rev. Lett.* **126** (2021) 201102.
- [17] S. Torii and P.S. Marrocchesi *Adv. Space Res.* **64** (2019) 2531.
- [18] S. Torii in *Proceedings of Science (ICRC2017) 1092*, 2017.
- [19] Y. Asaoka in *Proceedings of Science (ICRC2019) 001*, 2019.
- [20] P. Marrocchesi in *Proceedings of Science (ICRC2021) 010*, 2021.
- [21] O. Adriani et al. *Phys. Rev. Lett.* **119** (2017) 181101.
- [22] O. Adriani et al. *Phys. Rev. Lett.* **120** (2018) 261102.
- [23] O. Adriani et al. *Phys. Rev. Lett.* **128** (2022) 131103.
- [24] O. Adriani et al. *Phys. Rev. Lett.* **126** (2021) 241101.
- [25] CALET collaboration *Astroparticle Physics* **100** (2018) 29.
- [26] Y. Akaike in *Proceedings of Science (ICRC2015) 613*, 2015.
- [27] K. Kasahara in *Proc. of 24th ICRC*, vol. 1, p. 399, 1995.
- [28] J. Allison et al. *Nucl. Instrum. Methods Phys. Res., Sect. A* **835** (2016) 186.
- [29] Y. Asaoka et al. *Astroparticle Physics* **91** (2017) 1.
- [30] G. D’Agostini *Nucl. Instr. and Meth. A* **362** (1995) 487.
- [31] T. Adye in *Proc. of the PHYSTAT, CERN-2011-006*, 2011 [[arXiv:1105.1160](#)].
- [32] V. Grebenyuk et al. *arXiv:1809.07285 [astro-ph.HE]* (2018) .
- [33] J.J. Engelmann et al. *Astron. Astrophys.* **233** (1990) 96.
- [34] G. Minagawa *Astrophys. J.* **248** (1981) 847.
- [35] J.S. Young et al. *Astrophys. J.* **246** (1981) 1014.
- [36] A. Panov et al. *Bull. Russian Acad. Sci.* **73** (2009) 564.
- [37] M. Ave et al. *Astrophys. J.* **678** (2008) 262–273.
- [38] D. Müller et al. *Astrophys. J.* **374** (1991) 356.
- [39] M. Aguilar et al. *Phys. Rev. Lett.* **126** (2021) 041104.

Full Author List: CALET Collaboration

O. Adriani^{1,2}, Y. Akaike^{3,4}, K. Asano⁵, Y. Asaoka⁵, E. Berti^{2,6}, G. Bigongiari^{7,8}, W.R. Binns⁹, M. Bonghi^{1,2}, P. Brogi^{7,8}, A. Bruno¹⁰, N. Cannady^{11,12,13}, G. Castellini⁶, C. Checchia^{7,8}, M.L. Cherry¹⁴, G. Collazuol^{15,16}, G.A. de Nolfo¹⁰, K. Ebisawa¹⁷, A.W. Ficklin¹⁴, H. Fuke¹⁷, S. Gonzi^{1,2,6}, T.G. Guzik¹⁴, T. Hams¹¹, K. Hibino¹⁸, M. Ichimura¹⁹, K. Ioka²⁰, W. Ishizaki⁵, M.H. Israel⁹, K. Kasahara²¹, J. Kataoka²², R. Kataoka²³, Y. Katayose²⁴, C. Kato²⁵, N. Kawanaka²⁰, Y. Kawakubo¹⁴, K. Kobayashi^{3,4}, K. Kohri²⁶, H.S. Krawczynski⁹, J.F. Krizmanic¹², P. Maestro^{7,8}, P.S. Marrocchesi^{7,8}, A.M. Messineo^{8,27}, J.W. Mitchell¹², S. Miyake²⁸, A.A. Moiseev^{29,12,13}, M. Mori³⁰, N. Mori², H.M. Motz¹⁸, K. Munakata²⁵, S. Nakahira¹⁷, J. Nishimura¹⁷, S. Okuno¹⁸, J.F. Ormes³¹, S. Ozawa³², L. Pacini^{2,6}, P. Papini², B.F. Rauch⁹, S.B. Ricciarini^{2,6}, K. Sakai^{11,12,13}, T. Sakamoto³³, M. Sasaki^{29,12,13}, Y. Shimizu¹⁸, A. Shiomi³⁴, P. Spillantini¹, F. Stolzi^{7,8}, S. Sugita³³, A. Sulaj^{7,8}, M. Takita⁵, T. Tamura¹⁸, T. Terasawa⁵, S. Torii³, Y. Tsunesada^{35,36}, Y. Uchihori³⁷, E. Vannuccini², J.P. Wefel¹⁴, K. Yamaoka³⁸, S. Yanagita³⁹, A. Yoshida³³, K. Yoshida²¹, and W.V. Zober⁹

¹Department of Physics, University of Florence, Via Sansone, 1 - 50019, Sesto Fiorentino, Italy, ²INFN Sezione di Firenze, Via Sansone, 1 - 50019, Sesto Fiorentino, Italy, ³Waseda Research Institute for Science and Engineering, Waseda University, 17 Kikuicho, Shinjuku, Tokyo 162-0044, Japan, ⁴JEM Utilization Center, Human Spaceflight Technology Directorate, Japan Aerospace Exploration Agency, 2-1-1 Sengen, Tsukuba, Ibaraki 305-8505, Japan, ⁵Institute for Cosmic Ray Research, The University of Tokyo, 5-1-5 Kashiwa-no-Ha, Kashiwa, Chiba 277-8582, Japan, ⁶Institute of Applied Physics (IFAC), National Research Council (CNR), Via Madonna del Piano, 10, 50019, Sesto Fiorentino, Italy, ⁷Department of Physical Sciences, Earth and Environment, University of Siena, via Roma 56, 53100 Siena, Italy, ⁸INFN Sezione di Pisa, Polo Fibonacci, Largo B. Pontecorvo, 3 - 56127 Pisa, Italy, ⁹Department of Physics and McDonnell Center for the Space Sciences, Washington University, One Brookings Drive, St. Louis, Missouri 63130-4899, USA, ¹⁰Heliospheric Physics Laboratory, NASA/GSFC, Greenbelt, Maryland 20771, USA, ¹¹Center for Space Sciences and Technology, University of Maryland, Baltimore County, 1000 Hilltop Circle, Baltimore, Maryland 21250, USA, ¹²Astroparticle Physics Laboratory, NASA/GSFC, Greenbelt, Maryland 20771, USA, ¹³Center for Research and Exploration in Space Sciences and Technology, NASA/GSFC, Greenbelt, Maryland 20771, USA, ¹⁴Department of Physics and Astronomy, Louisiana State University, 202 Nicholson Hall, Baton Rouge, Louisiana 70803, USA, ¹⁵Department of Physics and Astronomy, University of Padova, Via Marzolo, 8, 35131 Padova, Italy, ¹⁶INFN Sezione di Padova, Via Marzolo, 8, 35131 Padova, Italy, ¹⁷Institute of Space and Astronautical Science, Japan Aerospace Exploration Agency, 3-1-1 Yoshinodai, Chuo, Sagami-hara, Kanagawa 252-5210, Japan, ¹⁸Kanagawa University, 3-27-1 Rokkakubashi, Kanagawa, Yokohama, Kanagawa 221-8686, Japan, ¹⁹Faculty of Science and Technology, Graduate School of Science and Technology, Hirosaki University, 3, Bunkyo, Hirosaki, Aomori 036-8561, Japan, ²⁰Yukawa Institute for Theoretical Physics, Kyoto University, Kitashirakawa Oiwake-cho, Sakyo-ku, Kyoto, 606-8502, Japan, ²¹Department of Electronic Information Systems, Shibaura Institute of Technology, 307 Fukasaku, Minuma, Saitama 337-8570, Japan, ²²School of Advanced Science and Engineering, Waseda University, 3-4-1 Okubo, Shinjuku, Tokyo 169-8555, Japan, ²³National Institute of Polar Research, 10-3, Midori-cho, Tachikawa, Tokyo 190-8518, Japan, ²⁴Faculty of Engineering, Division of Intelligent Systems Engineering, Yokohama National University, 79-5 Tokiwadai, Hodogaya, Yokohama 240-8501, Japan, ²⁵Faculty of Science, Shinshu University, 3-1-1 Asahi, Matsumoto, Nagano 390-8621, Japan, ²⁶Institute of Particle and Nuclear Studies, High Energy Accelerator Research Organization, 1-1 Oho, Tsukuba, Ibaraki, 305-0801, Japan, ²⁷University of Pisa, Polo Fibonacci, Largo B. Pontecorvo, 3 - 56127 Pisa, Italy, ²⁸Department of Electrical and Electronic Systems Engineering, National Institute of Technology (KOSEN), Ibaraki College, 866 Nakane, Hitachinaka, Ibaraki 312-8508, Japan, ²⁹Department of Astronomy, University of Maryland, College Park, Maryland 20742, USA, ³⁰Department of Physical Sciences, College of Science and Engineering, Ritsumeikan University, Shiga 525-8577, Japan, ³¹Department of Physics and Astronomy, University of Denver, Physics Building, Room 211, 2112 East Wesley Avenue, Denver, Colorado 80208-6900, USA, ³²Quantum ICT Advanced Development Center, National Institute of Information and Communications Technology, 4-2-1 Nukui-Kitamachi, Koganei, Tokyo 184-8795, Japan, ³³College of Science and Engineering, Department of Physics and Mathematics, Aoyama Gakuin University, 5-10-1 Fuchinobe, Chuo, Sagami-hara, Kanagawa 252-5258, Japan, ³⁴College of Industrial Technology, Nihon University, 1-2-1 Izumi, Narashino, Chiba 275-8575, Japan, ³⁵Graduate School of Science, Osaka Metropolitan University, Sugimoto, Sumiyoshi, Osaka 558-8585, Japan, ³⁶Nambu Yoichiro Institute for Theoretical and Experimental Physics, Osaka Metropolitan University, Sugimoto, Sumiyoshi, Osaka 558-8585, Japan, ³⁷National Institutes for Quantum and Radiation Science and Technology, 4-9-1 Anagawa, Inage, Chiba 263-8555, Japan, ³⁸Nagoya University, Furo, Chikusa, Nagoya 464-8601, Japan, ³⁹College of Science, Ibaraki University, 2-1-1 Bunkyo, Mito, Ibaraki 310-8512, Japan